ORGANIC CHEMISTRY FRONTIERS

RESEARCH ARTICLE

View Article Online
View Journal

Cite this: DOI: 10.1039/d5qo00673b

NCI-driven regioselectivity and enantioreversal in chiral phosphoric acid-catalyzed arylamine functionalization†

Zi-Hao Li,[a] Abing Duan *[b] and Shu-Yu Zhang *[a]

Non-covalent interactions (NCIs) have emerged as pivotal elements in asymmetric catalysis, enabling precise control over reactivity and selectivity in complex transformations. Despite their central role in designing catalytic systems, mechanistic understanding remains limited for reactions where NCIs concurrently govern regio- and enantioselectivity. The inherent complexity of CPA-catalyzed asymmetric reactions, characterized by diverse NCIs—particularly with arylamine substrates bearing multiple NCI-active motifs—presents formidable challenges for theoretical analysis and data-driven mechanistic modeling. This challenge becomes particularly pronounced when examining the enantioreversal phenomenon, where minute NCI perturbations orchestrate divergent catalytic pathways. Crucially, substrate-controlled enantioreversal operating independently of CPA groups modifications remain conspicuously undercharacterized in multi-selective reactions, particularly at the mechanistic level. In this study, we investigate three representative multi-site CPA-catalyzed asymmetric functionalizations of arylamines, utilizing detailed theoretical calculations to explore the influence of steric effects and NCIs, as well as the interplay between regioselectivity and enantioreversal. Our findings clarify the factors governing regioselectivity and enantioreversal, leading to a detailed elucidation of the mechanistic roles of key variables in existing frameworks. This work provides a robust theoretical foundation for optimizing CPA-catalyzed asymmetric reactions involving arylamines, while paving the way for future machine learning-driven advancements in this domain.

Received 23rd April 2025,
Accepted 22nd May 2025

DOI: 10.1039/d5qo00673b

rsc.li/frontiers-organic

Introduction

Non-covalent interactions (NCIs), though significantly weaker in strength compared to chemical bonds, play a pivotal role in diverse fields such as drug design, supramolecular chemistry, molecular biology, and materials science (Scheme 1A).[1,2] In organic catalysis, NCIs are central to catalytic system design, enabling substrate activation and selective control. The multivalent cooperativity and reversibility of these weakly bound systems unlock vast creative potential under suitable mechanistic guidance.[3–6] The advancement of synthetic strategies aiming for precise multi-selectivity control has elevated NCIs as pivotal elements in asymmetric catalyst design. While sustained exploration of NCI-mediated catalysis deepens mechanistic insights, it simultaneously drives the creation of highly selective and efficient systems. NCIs prediction/optimization has evolved from chemical intuition to quantum chemistry and machine learning-driven models, decoding molecular recognition and catalytic dynamics to guide targeted catalyst design.[7,8]

Chiral phosphoric acids (CPAs) are one of the most widely utilized asymmetric catalysts, featuring multiple tunable NCI-active sites that engage substrates *via* tailored NCIs to mediate diverse transformations.[9–11] While successful models exist to predict CPA-catalyzed enantioselectivity, theoretical investigations remain scarce for reactions where NCIs simultaneously govern regio- and enantioselectivity—particularly those involving intricate substrate–substrate NCIs.[12–14] The rare yet critical phenomenon of enantioreversal among analogous systems highlights how subtle perturbations in NCIs can dictate divergent reaction pathways, which predominantly occurs in scenarios involving CPA R-group modifications or asymmetric hydrogenation reactions, whereas substrate-controlled enantioreversal independent of CPA variations in multi-selective systems remains relatively underexplored, particularly in the realm of mechanistic studies.[15–21] In contrast, substrate-controlled enantioreversal—which operates independently of CPA variations in multi-selective systems—remains underexplored, particularly within mechanistic studies. Detailed mechanistic dissection of these edge cases is imperative to unravel the deci-

[a]State Key Laboratory of Synergistic Chem-Bio Synthesis, Shanghai Key Laboratory for Molecular Engineering of Chiral Drugs & School of Chemistry and Chemical Engineering, Shanghai Jiao Tong University, Shanghai 200240, P.R. China. E-mail: zhangsy16@sjtu.edu.cn
[b]College of Environmental Science and Engineering, Hunan University, Changsha 410082, China. E-mail: duanabing@hnu.edu.cn

† Electronic supplementary information (ESI) available. See DOI: https://doi.org/10.1039/d5qo00673b

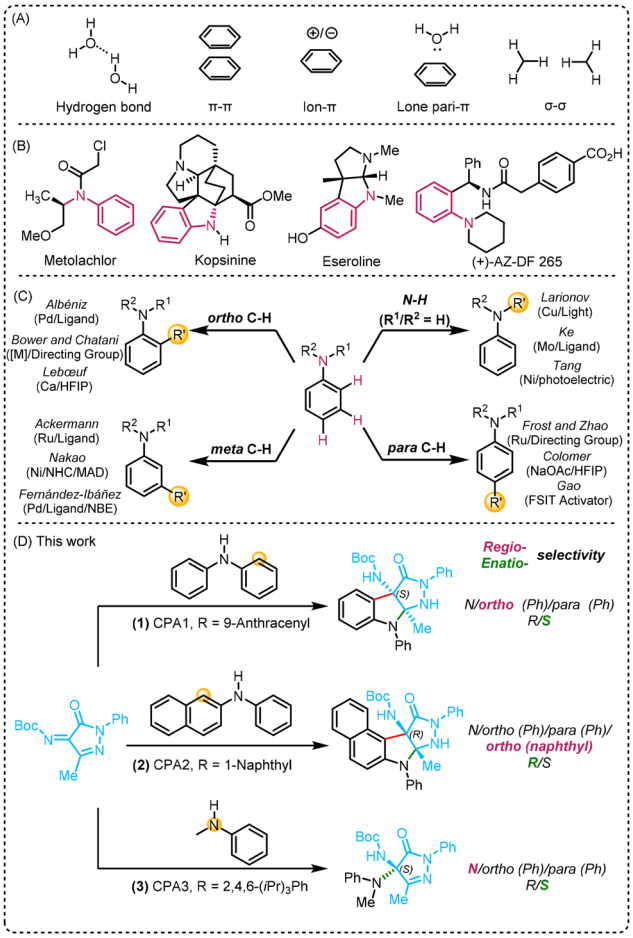

Scheme 1 (A) Common NCIs in organocatalysis. (B) Some important arylamine derivatives. (C) Some examples of selective functionalization reactions of arylamines. (D) Representative reactions in this work.

sive role of NCIs in CPA catalysis, thereby addressing critical gaps in current data-driven mechanistic frameworks.

Arylamines and their derivatives are pivotal substrates in synthetic chemistry, prized for their extensive applications in pharmaceuticals and functional materials (Scheme 1B).[22–25] Decades of research have focused on efficient strategies for their functionalization.[26–30] The inherent multiplicity of reactive sites within arylamines renders precise control over chemoselectivity and regioselectivity a central challenge in advancing these methodologies (Scheme 1C).[31–50] Arylamines containing N–H groups engage CPAs through hydrogen-bonding interactions, enabling activation while their aryl moieties direct site-specific asymmetric functionalization *via* π–π interactions with catalyst-derived aromatic systems. However, chemoselective and regioselective C–H functionalization of N–H-donor arylamines presents exceptional challenges due to: (i) competing reactivity at *ortho*/*meta*/*para* positions and nitrogen centers of arylamines; (ii) dual aryl motifs in most arylamines generating multiple NCIs networks and reactive sites; (iii) the dynamic interplay of hydrogen bonding and multiple π–π interactions obscuring mechanistic clarity; (iv) competitive N–H insertion pathways complicating product distribution.[51,52] The intricate interplay of NCIs and multi-reactive sites severely hinders mechanistic elucidation in CPA-catalyzed arylamine functionalization, while concurrent selectivity control imposes formidable computational demands for theoretical modeling.

Building upon our longstanding investigations into CPA-catalyzed asymmetric functionalization of arylamines,[53–59] three representative cases were identified where minor structural variations (single substituent modifications) induce dramatic regioselectivity switches and enantioreversal (Scheme 1D).[57,58] Herein, we aim to elucidate the mechanistic underpinnings of NCIs in these transformations through focused analysis of these model reactions. Through detailed theoretical calculations and analysis, we elucidate the potential reactivity of other unreacted sites and assess the quantitative influence of steric effects and weak interactions on regioselectivity and enantioreversal phenomena, providing in-depth insights into the factors governing these outcomes. Furthermore, we provide a detailed explanation of the mechanistic roles of the variables in existing models, discovering how regioselectivity and enantioselectivity are jointly determined by nucleophilicity at reaction sites and steric effects, and quantitatively assessing this through fitting of the corresponding intrinsic correlations.

Computational details

All of the calculations were performed with the Gaussian 16 package.[60] After the comparison of DFT methods (see the ESI† for details), the M06-2X functional with the standard 6-31G(d, p) basis set was used for the geometry optimizations in the gas phase.[61,62] Harmonic vibrational frequency calculations were carried out at the same level of theory for all of the stationary points to verify whether they are local minima or transition structures and to derive the thermal energy corrections. An extensive conformational search was performed by metadynamics simulations in the gas phase with the conformer–rotamer ensemble sampling (CREST) algorithm.[63] Additionally, empirical and model-based conformational searches were performed to ensure that the lowest energy conformers are discussed (see the ESI† for details). Distortion and interaction energies were computed at the M06-2X-D3/6-311+G (d,p) level.[64,65] Based on gas-phase optimized geometries, the solvent energy calculations were performed at the M06-2X-D3 functional with the 6-311+G(d,p) basis set with the SMD continuum solvation model in a respective solvent.[66] The analyses were conducted with Multiwfn and VMD programs.[67,68] All optimized structures were generated with VMD and CYLview.[69]

Results and discussion

Proposed catalytic cycle (Scheme 2)

For the reactions (1) and (2) in Scheme 1D, the first elementary step, TS-A, was most likely to occur through the common bifunctional activation mode of CPAs,[10,70–72] in which the proton was transferred from aniline to ketimine *via* consecu-

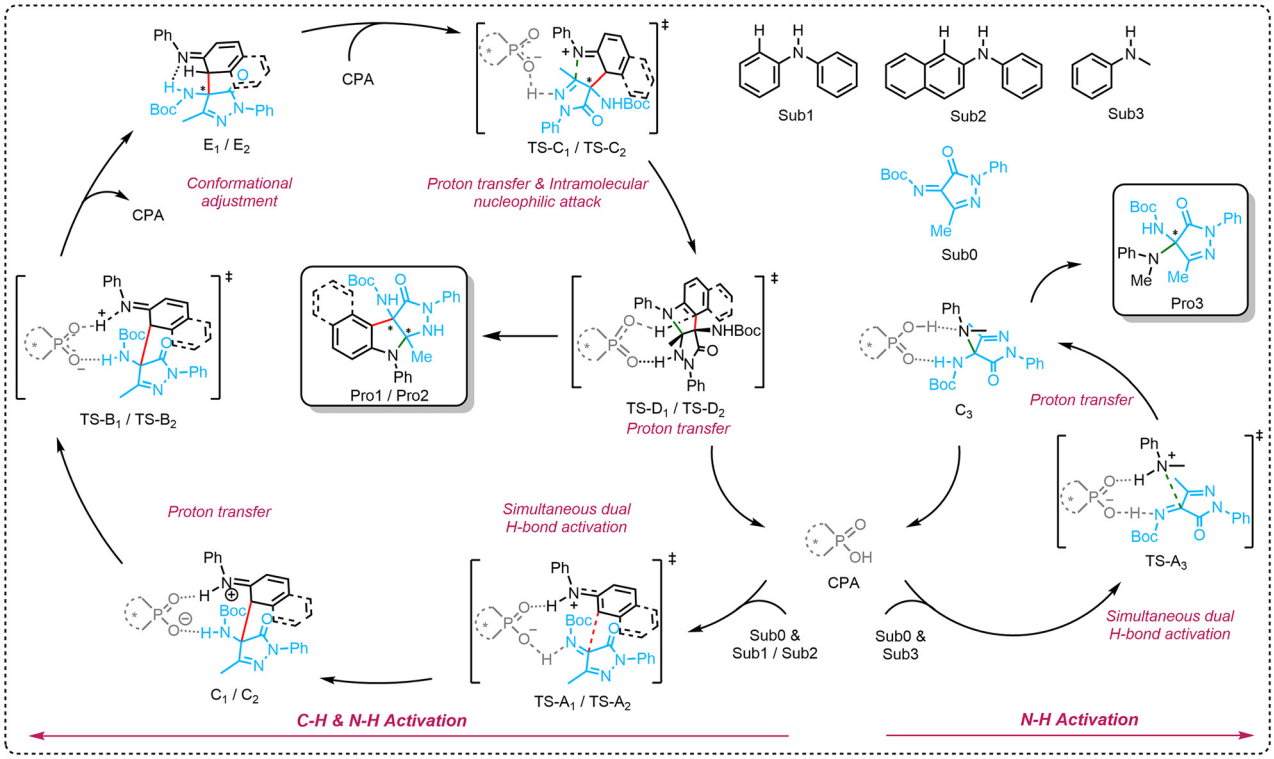

Scheme 2 Possible reaction pathways.

tive TS-B. Subsequently, to accomplish intramolecular cyclization, the arylamine parts of the intermediate needed to rotate around the newly formed C–C bond to the specific position, while CPA must move to the opposite side of the intermediate to activate the nitrogen atom in the pyrazolinone. This meant that CPA would first dissociate from *E* to adjust the conformation. Next, the reintroduction of CPA activated the C–N double bond in the pyrazolinone ring, facilitating the attack of the imine nitrogen of anilines *via* TS-C. Finally, through TS-D, proton transfer-induced regeneration of CPA, and re-aromatization of the Aryl, the product was obtained. As for reaction (3), the *N* atom of Sub3 was primarily proposed to attack the imine (Sub0) *via* TS-A_3 directly, with the dual-function activation assistance of CPA, to generate *N*,*N*′-acetals motif. Subsequently, the product was obtained through proton transfer. Based on the above proposals for these three reactions, we respectively selected the template substrates under the corresponding optimal conditions with catalysis as model reactions for calculation, as shown in Scheme 3.

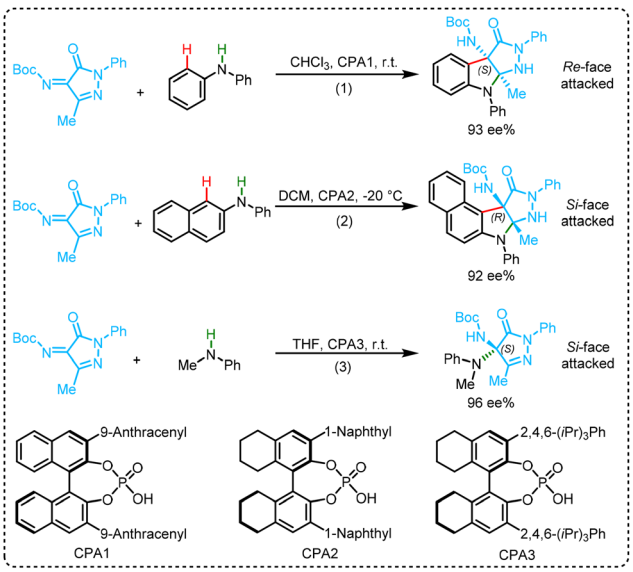

Scheme 3 Three CPA-catalyzed enantioselective reactions between pyrazolinone ketimines (Sub0) and (1) *N*-phenylaniline (Sub1); (2) *N*-phenyl-2-naphthylamines (Sub2); (3) *N*-methylaniline (Sub3).

Mechanism of the CPA-catalyzed [3 + 2] annulation between ketimines (Sub0) and *N*-phenylaniline (Sub1) (reaction 1)

With two phenyls of substrate Sub1, we first began our investigation on the reaction (1) for simple regioselectivity. As shown in Fig. 1, CPA1 sequentially interacted with the two substrates, first forming A_1, followed by the intermediates B_1 and B_1'. In B_1, Sub0 faced Sub1 with its *Re*-face, while in B_1', it faced with *Si*-face. Subsequently, with the bifunctional activation of CPA, the *ortho*-C-position of the phenyl in Sub1 would nucleophilically attack CPA-protonated Sub0 to form the first chiral center, which is the stereoselectivity-determining step. Based on the exploration of the model developed by Professor Reid and Professor Goodman,[12] the energy difference of the tran-

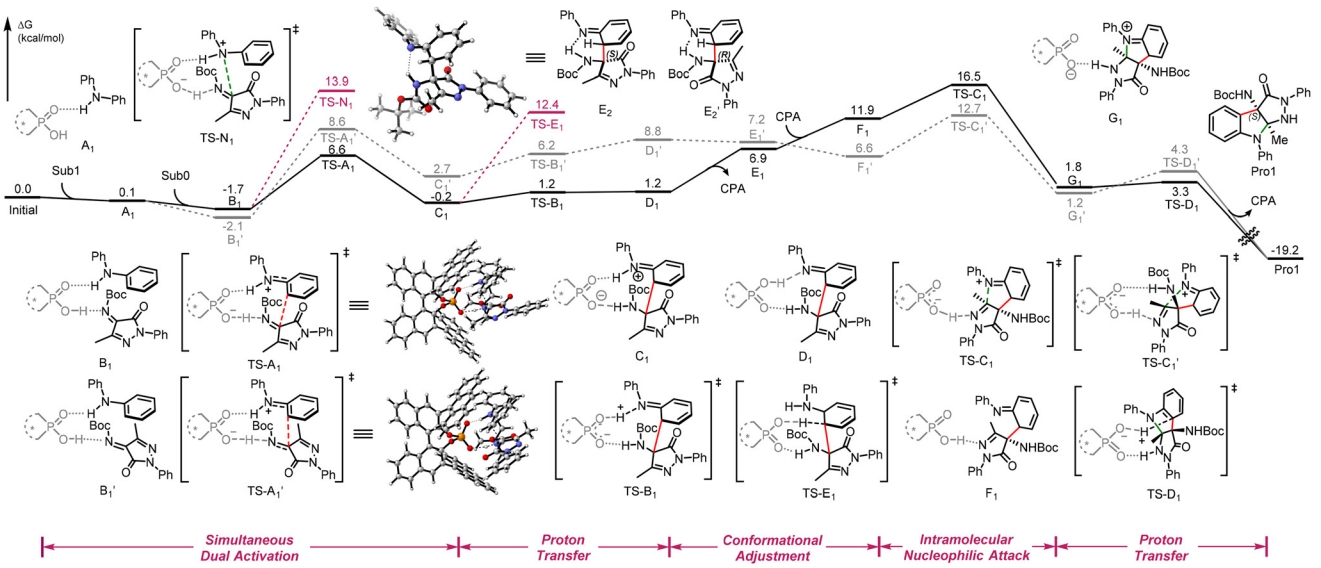

Fig. 1 Calculated Gibbs free energy profile of the reaction (1) between pyrazolinone ketimines (Sub0) and *N*-phenylaniline (Sub1). Energies are in kcal mol^{-1} and represent the relative free energies calculated in $CHCl_3$.

sition states (TS-A_1 and TS-A_1′) is 2.0 kcal mol^{-1} under Curtin–Hammett control, which is extremely close to experimental 95% ee value under the standard reaction condition (additional possible transition states based on Goodman's model are provided in the ESI†). The energy difference between TS-A_1 and TS-A_1′ may arise from the steric effects between the methyl group in Sub0 and the phenyl group on the same side in Sub1 (as shown in Fig. S5†).

Considering the regioselectivity, we also calculated the transition state that the N atom of *N*-phenylaniline attacks directly (TS-N_1), which is energetically unfavorable. With proton deficiency, the CPA anion tended to reprotonate from the coupling intermediate, leading to cleavage of N–H in *N*-phenylaniline *via* TS-B_1 and generating D_1. The higher energy barrier of deprotonation from phenyl by TS-E_1 indicated the impossibility of obtaining the simple coupling product, and the new imide group enforced the following intramolecular process. For the subsequent construction of the intramolecular C–N bond, the arylamine portion of the intermediate had to rotate approximately 180° around the C–C bond, while CPA needed to shift to the opposite side of the intermediate to activate the nitrogen in the pyrazolinone. Thus, the CPA was first dissociated to adjust conformation and form the intermediate E_1, and the reintroduction of CPA involved activating the C=N in the five-membered ring of ketimine by protonation, which facilitated the nucleophilic attack of the N atom of Sub1 *via* TS-C_1. Finally, the proton transfer *via* TS-D_1 leads to the product and the renewal of CPA.

Mechanism of the CPA-catalyzed [3 + 2] annulation between ketimines (A) and *N*-phenyl-2-naphthylamine (Sub2) (reaction 2)

In reaction (2), a similar process is illustrated in Fig. 2, but the chirality of the product Pro2 is opposite to that of Pro1. The two substrates sequentially bound to CPA, forming B_2 and B_2′. In B_2, Sub0 faced Sub2 with its *Si*-face, while in B_2′, it faced with *Re*-face. The higher energy of B_2 may arise from the steric effects between the Boc group in Sub0 and the phenyl group in Sub2 (as shown in Fig. S6†), which is largely offset in TS-A_2 due to the proximity of the two substrates on the opposite side. Subsequently, the reaction proceeded through nucleophilic attack *via* TS-A_2 and TS-A_2′, similar to reaction (1). Additionally, the transition state for the potential reaction site on the phenyl group was calculated *via* TS-P_2, which proved unfavorable in terms of energy barrier. A detailed analysis of regioselectivity and enantioreversal is provided in the following text.

Mechanism of the CPA-catalyzed chiral *N*-alkylation between ketimines (Sub0) and *N*-methylaniline (Sub3) (reaction 3)

In reaction (3), the only elementary step occurred *via* TS-A_3 through common bifunctional activation of CPAs, with proton transfer happening simultaneously. In B_3, Sub0 faced Sub3 with its *Si*-face, while in B_3′, it faced with *Re*-face. Considering regioselectivity, we also calculated the transition state for the potential reaction site on the phenyl group *via* TS-P_3, which proved to be extremely unfavourable for the *N*-alkylation aniline process in energy. The shift of the reaction site to N may be due to the significant reduction in steric hindrance when an aryl group is converted to a methyl group. A detailed analysis of regioselectivity and enantioreversal is also provided in the following text.

Origins and analysis of regioselectivity-determining step

Before utilizing existing models to predict the absolute configuration of chiral products, it is essential to first assess the regioselectivity of the reactions, as the reaction sites are impor-

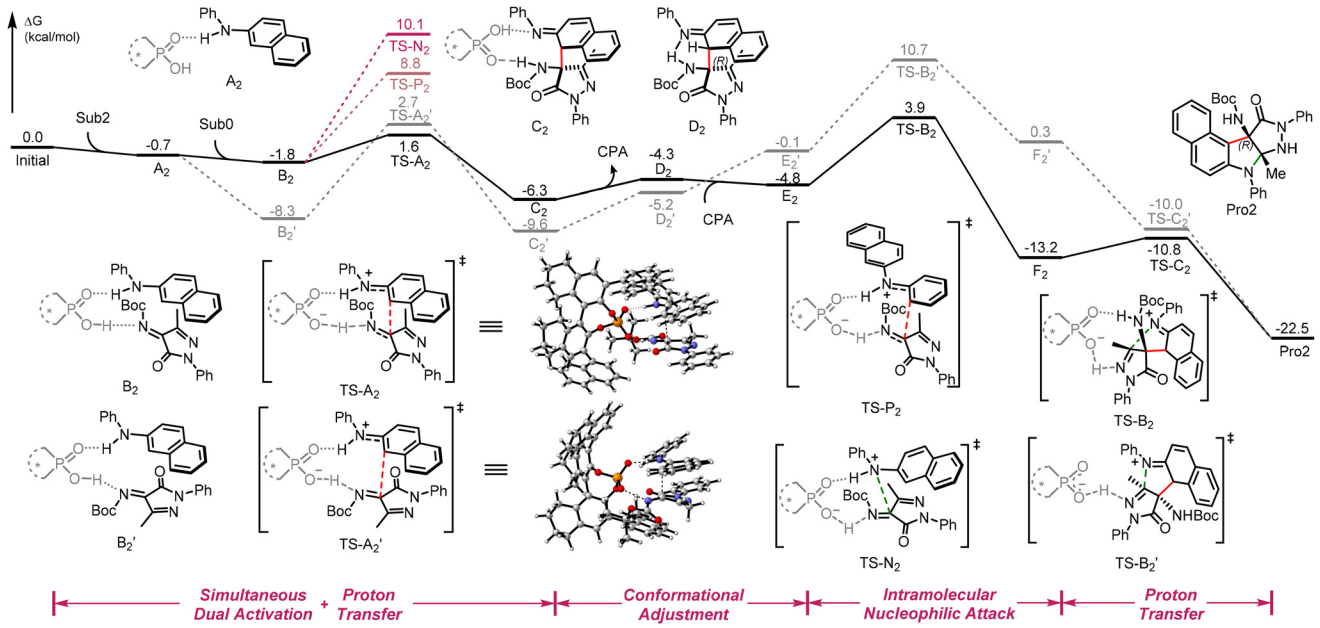

Fig. 2 Calculated Gibbs free energy profile of the reaction (2) between pyrazolinone ketimines (Sub0) and *N*-phenyl-2-naphthylamine (Sub2). Energies are in kcal mol^{-1} and represent the relative free energies calculated in DCM.

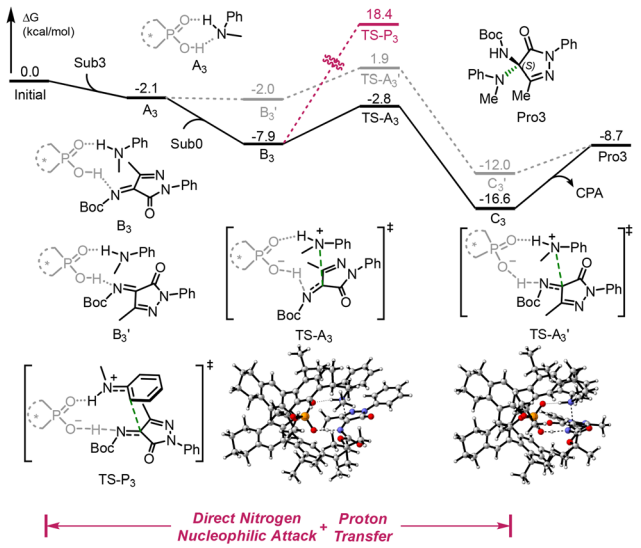

Fig. 3 Calculated Gibbs free energy profile of the reaction (3) between pyrazolinone ketimines (Sub0) and *N*-methylaniline (Sub3). Energies are in kcal mol^{-1} and represent the relative free energies calculated in THF.

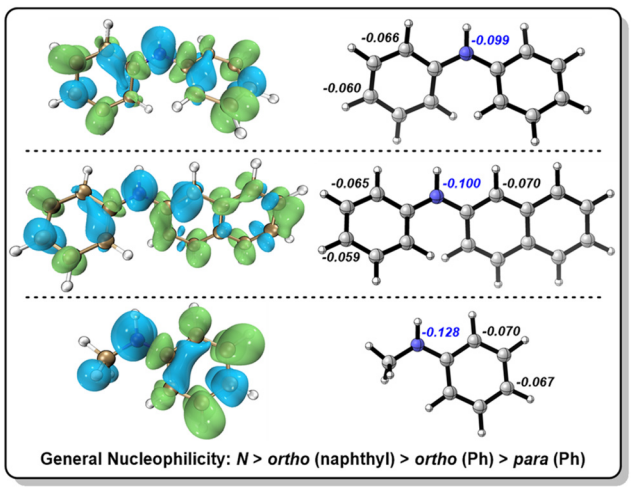

Fig. 4 Orbital-weighted dual descriptor isosurfaces (value = ±0.001) calculated by Multiwfn using a width of the Gaussian function (Δ) of 0.1 a.u. for substrates in the three reactions. Green/blue (positive/negative values) represent electrophilic attack/nucleophilic susceptibility (left). The 3D structures of substrates in three reactions. The number represents the highest Hirshfeld charges of the *N* atom and the *ortho*/*para* *C* atom of the aryls group (right).

tant considerations for subsequent analysis of enantioselectivity.

As shown in Fig. 1–3, the regioselectivity-determining step in these three reactions occurs during the first nucleophilic attack step activated by CPA. To reveal the origin, we first analysed the nucleophilic features of arylamine substrates in these reactions. As depicted in Fig. 4 (left), the N-position of these three arylamines owned the strongest nucleophilicity compared to other reaction sites, as indicated by the analysis of the orbital-weighted dual descriptor.[73] Additionally, the *ortho* position of the phenyl groups in Sub1/Sub2 and the C1-position of naphthyl in Sub2 display weaker nucleophilic susceptibility than the N-position, with the *para* position of the phenyl groups following closely behind. For Sub2, which involves two different aryl groups in term of selectivity, the naphthyl group is slightly more nucleophilic than phenyl group. The same

nucleophilic trend is also evident from the Hirshfeld charge distribution shown in Fig. 4 (right).

Although the strongest nucleophilicity is present, reactions (1) and (2) did not achieve a direct nucleophilic attack of N-position in the first step. To explore the driving force behind the transfer of the reaction site, we conducted distortion/interaction analysis to investigate the first transition states of all pathways in these three reactions, as shown in Scheme 4.[74–76] For reactions (1) and (2), the distortion energy of CPA ($\Delta E_{\text{dis-CPA}}$) increased significantly when the N-position attacked the imine (Scheme 4A and B). However, the backbone of CPAs didn't undergo significant changes, as indicated by RMSD calculation (Table 1), suggesting that the primary contributor to $\Delta E_{\text{dis-CPA}}$ was proton transfer.

To further analyze the proton transfer character, the relationship between bond length and $\Delta E_{\text{dis-CPA}}$ has also been statistically analyzed, as presented in Table 1 and fitted in Scheme 5. The good fitting results across different arylamines and CPA ranges indicated that the strong degree of proton transfer from CPAs to imine substantially increases the distortion energies of the CPAs, leading to unfavorable transition

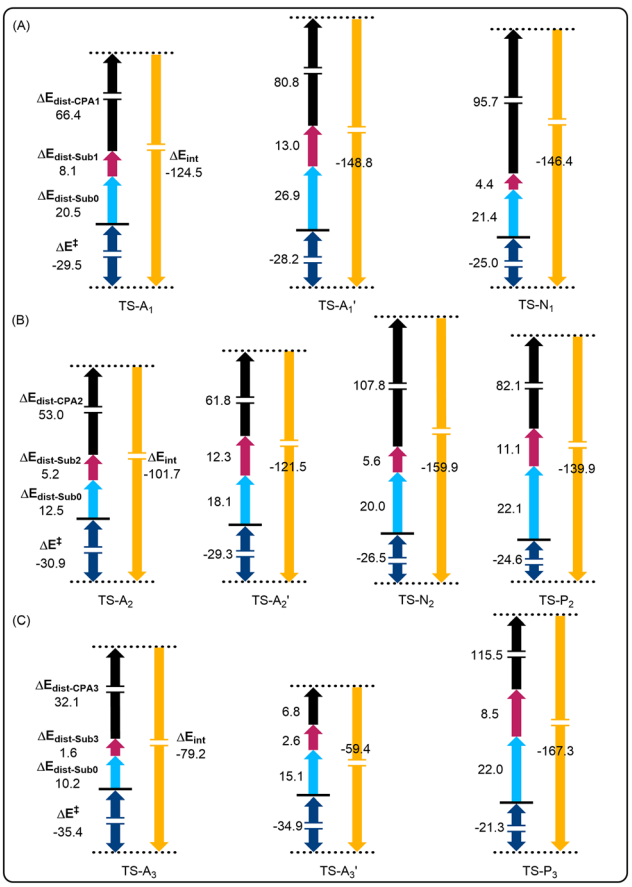

Scheme 4 Distortion, interaction, and activation energies in the reactions (kcal mol^{-1}): (A) TS-A_1, TS-A_1′, TS-N_1 in reaction 1; (B) TS-A_2, TS-A_2′, TS-N_2 and TS-P_2 in reaction 2; (C) TS-A_3, TS-A_3′, TS-P_3 in reaction 3. All transition states are separated into three distorted fragments (CPAs, arylamines, and imines).

Table 1 Structural characteristics of transition states[a]

TS ref	RMSD[b]	O-H[c]	H···N[d]	Distance (CPA + imines)[e]	Distance (CPA + arylamines)[f]
TS-A_1	0.25	1.50	1.09	2.59	2.70
TS-A_1′	2.50	1.58	1.07	2.65	2.61
TS-N_1	0.35	1.74	1.05	**2.79**	**2.92**
TS-A_2	0.78	1.39	1.14	2.53	2.70
TS-A_2′	0.36	1.43	1.10	2.53	2.62
TS-N_2	0.93	1.86	1.04	**2.90**	**2.85**
TS-P_2	0.72	1.60	1.06	2.66	2.65
TS-A_3	0.42	1.25	1.22	2.47	2.77
TS-A_3′	0.61	1.05	1.51	2.56	2.77
TS-P_3	0.44	1.88	1.03	**2.91**	**2.84**

[a] All distance units are in Å. [b] The RMSD of the CPAs' backbone calculated by VMD in comparison to the initial states. [c] The O–H distance of CPAs. [d] The distance between hydroxyl H of CPAs and the terminal N of imines. [e] The sum of O–H and H···N=C distance between CPA and imines. [f] The sum of O···H and H–N distance between CPA and arylamines.

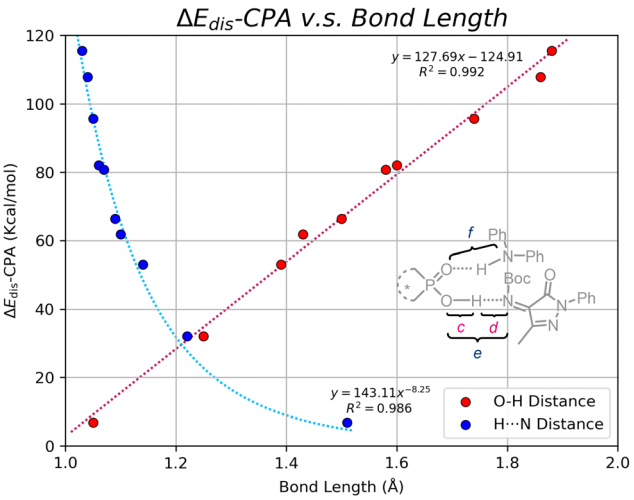

Scheme 5 The relationship between distortion energies of CPAs and bond length of O–H and H···N in Table 1.

states at the reaction sites. Based on the general principles governing this type of CPA-catalyzed reaction, we observed that the transition states for the direct *N*-alkylation of bisarylamines in reactions (1) and (2) show an increased requirement for proton transfer. This was particularly evident when considering variations in the skeletons and R-groups of the CPAs, which results in longer O–H distance and shorter H···N distance, as shown in Table 1. These structural characteristics of the transition states created a greater distance between CPAs and imines, allowing sufficient space for amines with two aryl groups (Sub1 and Sub2) to nucleophilically attack the N atom. The same distance trend was also observed between CPAs and arylamines.

In summary, the structural analysis of the transition states revealed that bisarylamines require the largest steric space to effectively attack the imine *via* the most nucleophilic nitrogen. This need for steric accommodation significantly increases the

energy barriers, far outweighing any benefits derived from enhanced nucleophilicity. Therefore, the reaction (1) and (2) tended to favor sites with comparatively weaker nucleophilicity, largely due to the significant influence of steric hindrance. The interplay between steric hindrance and nucleophilicity cannot be directly observed in the transition state, as the output reflects the optimized final results. As for reaction (3), steric hindrance was not an issue because one of the substituents is a methyl group. Moreover, the presence of additional weak interactions in the system favored the direct nucleophilic attack on nitrogen. As shown in Fig. 5, the π–π stacking interactions between the phenyl groups of the two substrates played a crucial role in localization. This was further corroborated by control experiments, which demonstrated that a racemic product was obtained using dimethylamine.[58] Additionally, the compatibility of the weak interactions between the methyl groups of two substrates and the iPr groups of CPA is notably high: the methyl groups can precisely fit into the cavity formed by the iPr groups of CPA, significantly enhancing the enantioselectivity of the reaction (3), which may contribute to the catalytic generality of 2,4,6-iPr (TRIP) group.[77]

Summarized as a simple empirical model, the regioselectivity is primarily influenced by the nucleophilicity of the reaction site in arylamines, with a significant impact from steric effects of CPAs. While pyrazolinone ketimine acts as an electrophile, the reaction site for diarylamines is the carbon with the highest nucleophilicity on the aromatic ring. Additionally, methylaniline would react directly with the nitrogen due to reduced steric hindrance.

Origins and analysis of the stereodivergent phenomenon

As shown in Scheme 2, the absolute configuration of the products in reaction (1) was opposite to that in reactions (2) and (3), no matter what kind of CPA the reaction used. To explore this stereo-divergent phenomenon, we focused on the first transition state, which is the stereodetermining step in all three reactions. We carefully analyzed the transition state structures of the corresponding enantiomers based on Goodman's model, as illustrated in Fig. S1–S3.†

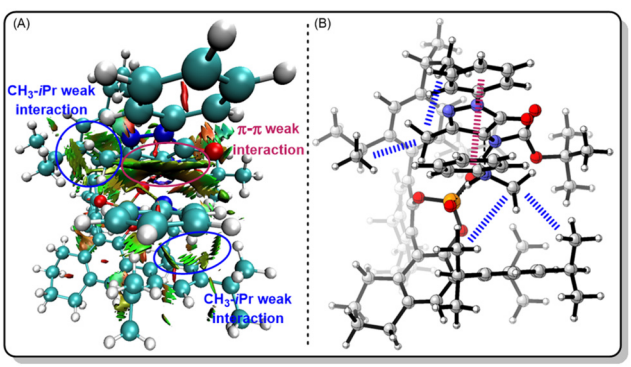

Fig. 5 (A) Noncovalent interactions (NCIs) analysis of TS-A_3 in reaction (3). (B) 3D structure of TS-A_3 in reaction (3).

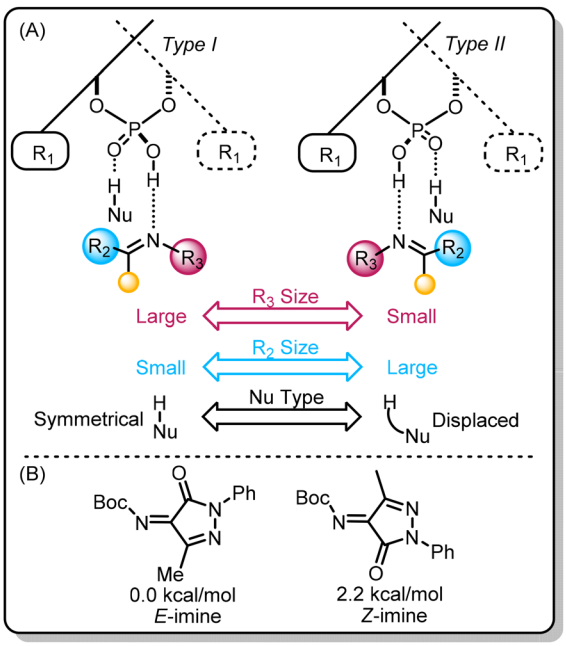

Fig. 6 (A) The practical model by Goodman for predicting the stereochemistry of CPA-catalyzed reactions of imines. (B) The energy difference between the *Z* and *E* configurations of imine Sub0 indicated that methyl group is a small R_2 group.

Starting with the simplest reaction (3), the imine substrate features a large R_3 group (*Boc* group),[78] a small R_2 group (methyl group), and a symmetrical nucleophile type. The hydrogen bond connecting the nucleophile to the catalyst aligns with the nucleophilic site. Guided by the model (Fig. 6A) and the regioselective model summarized in the previous section, the stereochemical outcome of reaction (3) can be easily analyzed, resulting in favorable configurations *via* *Type I E* with the lowest energy, which leads to the attack on the *Si*-face of Sub0. The experimental and computational results were also consistent with the model predictions, as shown in Table 2.

In reaction (1), the nucleophile shifts from symmetrical to displace type, leading to a favorable configuration of *Type II* with lower energy *E*-configuration.[79,80] The experimental and computational findings were also in agreement with the model's predictions. Notably, based on the weak interaction

Table 2 Ranking of transition state models[a]

Reaction	1[b]	2	3	4
(1)	***Type II E***	*Type I Z*	*Type II Z*	*Type I E*
(2)	***Type II Z***	*Type I Z*	*Type II E*	*Type I E*
(3)	***Type I E***	*Type I Z*	*Type II E*	*Type II Z*
	Energy barrier: low to high			

[a] The transition state energies increase from low to high, corresponding to states 1–4. For more details on transition state structures, see the ESI.† [b] The attack direction of the favourable transition state in reaction (2) and (3) is the same, while it's opposite in reaction (1).

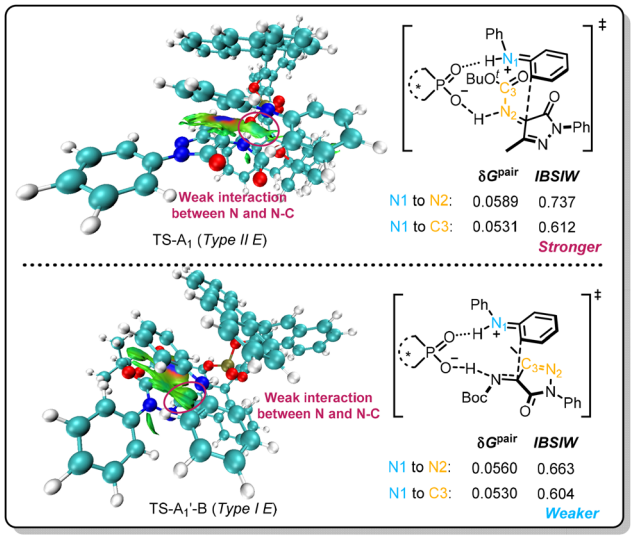

Fig. 7 The independent gradient model is based on Hirshfeld partition (IGMH) analysis between two substrates (Sub0 and Sub1) of reaction (1) in TS-A_1 and TS-A_1′-B. The sign(λ_2)ρ colored isosurfaces were plotted with 0.01 isovalue by VMD. The atomic pair δg index (δG^{pair}) and intrinsic bond strength index for weak interaction (IBSIW) are also calculated.

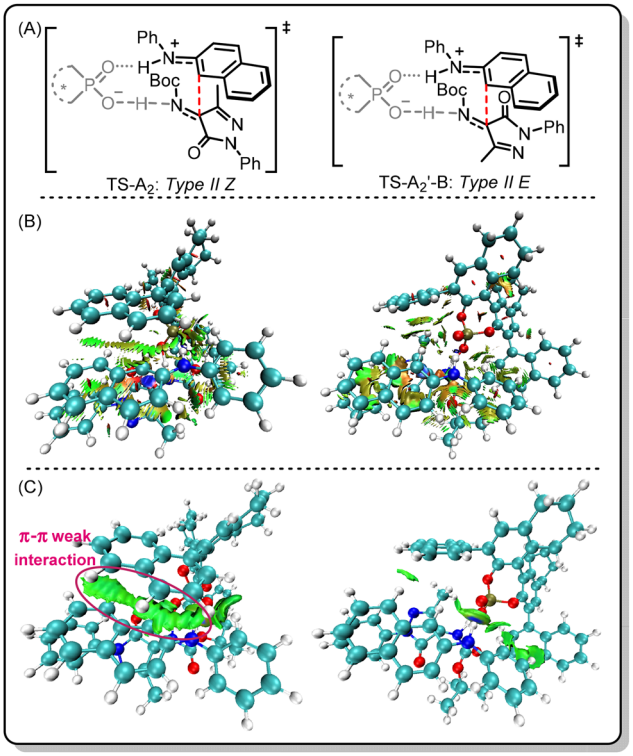

Fig. 8 (A) Transition state structure of TS-A_2 (*Type II Z*) and TS-A_2′-B (*Type II E*) in reaction (2). (B) Noncovalent interactions (NCI) analysis of corresponding transition states. (C) The independent gradient model based on Hirshfeld partition (IGMH) analysis between CPA and arylamine (B-2) of reaction (2) in TS-A_2 and TS-A_2′-B. The sign(λ_2)ρ colored isosurfaces were plotted with 0.005 isovalue by VMD.

analysis, the energy flip between *Type I* and *Type II* was quite intriguing in reaction (1): the amino nitrogen of Sub1 exhibits a strong weak interaction with the amide bond atom pair, as shown in Fig. 7. Due to the dual functional activation of CPAs, the N1 of arylamine and N2–C3 of imine became negatively and positively in charged, respectively, creating a specific weak interaction between the two substrates. When comparing the atomic pair δg index (δG^{pair}) and the intrinsic bond strength index for weak interaction (IBSIW) between *Type I E* to *Type II E* (TS-A_1 & TS-A_1′-B, Fig. 7 and Fig. S1†),[81] the weak interaction is stronger between N1 and amide N2–C3 atom pair in TS1 than between N1 and the double bond N2–C3 atom pair in TS-A_1′-B. This stronger interaction leads to the lower energy of *Type II E*. In short, due to the previously discussed steric hindrance effects, the change of nucleophilic site in reaction (1) favors *Type II* through a special weak interaction, which alters the absolute configuration compared to reaction (3). These specific weak interactions between substrates shed light on the potential mechanisms underlying the TS type conversion in the model as the nucleophile type changes, which leads to the attack on the *Re*-face of Sub0.

In reaction (2), attention focused on the reason for the advantage of *Z*-configuration, which led to a change in the nucleophilic attack direction. As shown in Fig. S4,† the advantage of *Type II* also stemmed from the same special weak interaction as observed in reaction (1), consistent with the model presented in Fig. 6 for the displaced nucleophile type. Regarding the overturn from *E*- to *Z*-configuration, NCI analysis (Fig. 8B) indicated that the π–π stacking weak interaction between the naphthyl group of Sub2 and the pyrazolinone part with phenyl of Sub0 led to excellent coplanarity of these two groups.[82] This characteristic between substrates maintained a relatively fixed orientation for the naphthyl group, blocking the π–π stacking interaction between the naphthyl groups of Sub2 and CPA in the *E*-configuration (Fig. 8C). In *Z*-configuration, the π–π stacking weak interaction performed exceptionally well, lowering the energy barrier of TS1 and ultimately leading to a conformational flip, which leads to the attack on the *Si*-face of Sub0.

Compared to the biphenyl group in Sub1, the conjugated region of the naphthyl group in Sub2 is farther, allowing it to engage in π–π stacking interactions with the more distant phenyl group in Sub0, which favors the *Z*/*E* flip. This is also the reason why reaction (2) undergoes a flip compared to reaction (1). The conversion of *E*/*Z*-configuration in imines induced by weak interactions is a noteworthy phenomenon associated with arylamines in these reactions, serving as an effective complement and advancement to the enantioselective prediction model.

In brief, compared to the representative reaction (3), the change of reaction site in reaction (1) led to an additional weak interaction between substrates, causing the model to shift from *Type I* to *Type II*, which led to chiral reversal. In reaction (2), the coplanarity of the substrates caused by π–π stacking influenced the weak interaction between CPA and the naphthyl group of Sub2, creating an energetically disadvantageous *E*-configuration that transformed into *Z*-configuration, resulting in another chiral reversal. Overall, we validated the

patterns of how changes in nucleophile types influence chirality within the existing model and further elucidated the underlying mechanistic reasons for the transitions between the models. Considering the structural coordinates of substrate–CPA complexes formed *via* hydrogen bonding, the relative spatial positions and orientations of π-functional groups can guide the quantification of NCIs.[83] These interactions can be characterized using computational descriptors and encoded into machine learning models to enable the modeling and prediction of regioselectivity and enantioreversal.[84,85]

Conclusions

In summary, we address the complexities of regioselectivity and stereoselectivity in CPA-catalyzed asymmetric functionalization of arylamines by examining three representative reactions through detailed DFT calculations and theoretical analysis. This work led to the development of a mechanistic understanding of regioselectivity and enantioreversal in the context of NCIs, revealing that these outcomes under similar conditions are governed by the interplay between nucleophilicity and steric effects. Furthermore, the research synthesizes existing models to validate enantioselectivity, demonstrating how intermolecular interactions influence chirality. Our findings not only establish a robust theoretical foundation for using NCIs to optimize CPA-catalyzed asymmetric reactions, but also pave the way for future applications and advancements in data-driven theoretical research and model development.

Data availability

The data supporting this article have been included as part of the ESI.†

Conflicts of interest

There are no conflicts to declare.

Acknowledgements

This work was supported by the National Key Research & Development Program of China (2022YFC2703400), the Shanghai Key Laboratory for Molecular Engineering of Chiral Drugs (No. SMECD2024003), the Science and Technology Innovation Program of Hunan Province (2024RC3077) and the Changsha Natural Science Foundation (kq2402056).

References

1 A. S. Mahadevi and G. N. Sastry, Cooperativity in Noncovalent Interactions, *Chem. Rev.*, 2016, **116**, 2775–2825.
2 S. Jena, J. Dutta, K. D. Tulsiyan, A. K. Sahu, S. S. Choudhury and H. S. Biswal, Noncovalent interactions in proteins and nucleic acids: beyond hydrogen bonding and pi-stacking, *Chem. Soc. Rev.*, 2022, **51**, 4261–4286.
3 A. J. Neel, M. J. Hilton, M. S. Sigman and F. D. Toste, Exploiting non-covalent pi interactions for catalyst design, *Nature*, 2017, **543**, 637–646.
4 H. J. Davis and R. J. Phipps, Harnessing non-covalent interactions to exert control over regioselectivity and site-selectivity in catalytic reactions, *Chem. Sci.*, 2017, **8**, 864–877.
5 Y. Kuninobu, Non-Covalent Interaction-Controlled Site-Selective C-H Transformations, *Chem. Rec.*, 2023, **23**, e202300149.
6 J. Chen, H. Wei, I. D. Gridnev and W. Zhang, Weak Attractive Noncovalent Interactions in Metal-Catalyzed Asymmetric Hydrogenation, *Angew. Chem., Int. Ed.*, 2025, e202425589, DOI: **10.1002/anie.202425589**.
7 S. E. Wheeler, T. J. Seguin, Y. Guan and A. C. Doney, Noncovalent Interactions in Organocatalysis and the Prospect of Computational Catalyst Design, *Acc. Chem. Res.*, 2016, **49**, 1061–1069.
8 F. D. Toste, M. S. Sigman and S. J. Miller, Pursuit of Noncovalent Interactions for Strategic Site-Selective Catalysis, *Acc. Chem. Res.*, 2017, **50**, 609–615.
9 D. Parmar, E. Sugiono, S. Raja and M. Rueping, Complete field guide to asymmetric BINOL-phosphate derived Bronsted acid and metal catalysis: history and classification by mode of activation; Bronsted acidity, hydrogen bonding, ion pairing, and metal phosphates, *Chem. Rev.*, 2014, **114**, 9047–9153.
10 R. Maji, S. C. Mallojjala and S. E. Wheeler, Chiral phosphoric acid catalysis: from numbers to insights, *Chem. Soc. Rev.*, 2018, **47**, 1142–1158.
11 I. O. Betinol, Y. Kuang, B. P. Mulley and J. P. Reid, Controlling Stereoselectivity with Noncovalent Interactions in Chiral Phosphoric Acid Organocatalysis, *Chem. Rev.*, 2025, **125**(8), 4184–4286.
12 J. P. Reid, L. Simon and J. M. Goodman, A Practical Guide for Predicting the Stereochemistry of Bifunctional Phosphoric Acid Catalyzed Reactions of Imines, *Acc. Chem. Res.*, 2016, **49**, 1029–1041.
13 J. P. Reid and M. S. Sigman, Holistic prediction of enantioselectivity in asymmetric catalysis, *Nature*, 2019, **571**, 343–348.
14 A. F. Zahrt, J. J. Henle, B. T. Rose, Y. Wang, W. T. Darrow and S. E. Denmark, Prediction of higher-selectivity catalysts by computer-driven workflow and machine learning, *Science*, 2019, **363**, 247.
15 Q. Kang, Z. A. Zhao and S. L. You, Asymmetric transfer hydrogenation of beta,gamma-alkynyl alpha-imino esters by a Bronsted acid, *Org. Lett.*, 2008, **10**, 2031–2034.
16 T. Marcelli, P. Hammar and F. Himo, Phosphoric acid catalyzed enantioselective transfer hydrogenation of imines: a density functional theory study of reaction mechanism and the origins of enantioselectivity, *Chemistry*, 2008, **14**, 8562–8571.

17 N. Li, X. H. Chen, J. Song, S. W. Luo, W. Fan and L. Z. Gong, Highly enantioselective organocatalytic Biginelli and Biginelli-like condensations: reversal of the stereochemistry by tuning the 3,3′-disubstituents of phosphoric acids, *J. Am. Chem. Soc.*, 2009, **131**, 15301–15310.
18 Q. Gu, Z. Q. Rong, C. Zheng and S. L. You, Desymmetrization of cyclohexadienones via Bronsted acid-catalyzed enantioselective oxo-Michael reaction, *J. Am. Chem. Soc.*, 2010, **132**, 4056–4057.
19 S. G. Wang, Q. Yin, C. X. Zhuo and S. L. You, Asymmetric dearomatization of beta-naphthols through an amination reaction catalyzed by a chiral phosphoric acid, *Angew. Chem., Int. Ed.*, 2015, **54**, 647–650.
20 A. Changotra, S. Das and R. B. Sunoj, Reversing Enantioselectivity Using Noncovalent Interactions in Asymmetric Dearomatization of beta-Naphthols: The Power of 3,3′ Substituents in Chiral Phosphoric Acid Catalysts, *Org. Lett.*, 2017, **19**, 2354–2357.
21 Z.-W. Qiu, L. Long, Z.-Q. Zhu, H.-F. Liu, H.-P. Pan, A.-J. Ma, J.-B. Peng, Y.-H. Wang, H. Gao and X.-Z. Zhang, Asymmetric Three-Component Reaction to Assemble the Acyclic All-Carbon Quaternary Stereocenter via Visible Light and Phosphoric Acid Catalysis, *ACS Catal.*, 2022, **12**, 13282–13291.
22 A. Bartolini, G. Renzi, A. Galli, P. M. Aiello and R. Bartolini, Eseroline: a new antinociceptive agent derived from physostigmine with opiate receptor agonist properties. Experimental in vivo and in vitro studies on cats and rodents, *Neurosci. Lett.*, 1981, **25**, 179–183.
23 M. G. Garrino and J. C. Henquin, Highly potent and stereoselective effects of the benzoic acid derivative AZ-DF 265 on pancreatic beta-cells, *Br. J. Pharmacol.*, 1988, **93**, 61–68.
24 P. J. O'Connell, C. T. Harms and J. R. F. Allen, Metolachlor, S-metolachlor and their role within sustainable weed-management, *Crop Prot.*, 1998, **17**, 207–212.
25 M. J. Tan, C. Yin, C. P. Tang, C. Q. Ke, G. Lin and Y. Ye, Antitussive indole alkaloids from Kopsia hainanensis, *Planta Med.*, 2011, **77**, 939–944.
26 C. S. Yeung and V. M. Dong, Catalytic dehydrogenative cross-coupling: forming carbon-carbon bonds by oxidizing two carbon-hydrogen bonds, *Chem. Rev.*, 2011, **111**, 1215–1292.
27 L. Ackermann, Carboxylate-assisted ruthenium-catalyzed alkyne annulations by C-H/Het-H bond functionalizations, *Acc. Chem. Res.*, 2014, **47**, 281–295.
28 H. Jia, Z. Tan and M. Zhang, Reductive Functionalization of Pyridine-Fused N-Heteroarenes, *Acc. Chem. Res.*, 2024, **57**, 795–813.
29 L.-W. Qi, T. Rogge, K. N. Houk and Y. Lu, Iridium nitrenoid-enabled arene C–H functionalization, *Nat. Catal.*, 2024, **7**, 934–943.
30 F. C. Raps, A. Rivas-Souchet, C. M. Jones and T. K. Hyster, Emergence of a distinct mechanism of C-N bond formation in photoenzymes, *Nature*, 2025, **637**, 362–368.
31 I. Colomer, Hydroarylation of Alkenes Using Anilines in Hexafluoroisopropanol, *ACS Catal.*, 2020, **10**, 6023–6029.
32 P. Cooper, G. E. M. Crisenza, L. J. Feron and J. F. Bower, Iridium-Catalyzed alpha-Selective Arylation of Styrenes by Dual C-H Functionalization, *Angew. Chem., Int. Ed.*, 2018, **57**, 14198–14202.
33 A. Dey, S. Agasti and D. Maiti, Palladium catalysed meta-C-H functionalization reactions, *Org. Biomol. Chem.*, 2016, **14**, 5440–5453.
34 U. Dutta and D. Maiti, Emergence of Pyrimidine-Based meta-Directing Group: Journey from Weak to Strong Coordination in Diversifying meta-C-H Functionalization, *Acc. Chem. Res.*, 2022, **55**, 354–372.
35 U. Dutta, S. Maiti, T. Bhattacharya and D. Maiti, Arene diversification through distal C(sp(2))-H functionalization, *Science*, 2021, **372**, 701.
36 S. M. Khake and N. Chatani, Rhodium(III)-Catalyzed Oxidative C–H Alkylation of Aniline Derivatives with Allylic Alcohols To Produce β-Aryl Ketones, *ACS Catal.*, 2022, **12**, 4394–4401.
37 J. A. Leitch, C. L. McMullin, A. J. Paterson, M. F. Mahon, Y. Bhonoah and C. G. Frost, Ruthenium-Catalyzed para-Selective C-H Alkylation of Aniline Derivatives, *Angew. Chem., Int. Ed.*, 2017, **56**, 15131–15135.
38 J. Li, S. Warratz, D. Zell, S. De Sarkar, E. E. Ishikawa and L. Ackermann, N-Acyl Amino Acid Ligands for Ruthenium(II)-Catalyzed meta-C-H tert-Alkylation with Removable Auxiliaries, *J. Am. Chem. Soc.*, 2015, **137**, 13894–13901.
39 W. Li, M. Huang, J. Liu, Y.-L. Huang, X.-B. Lan, Z. Ye, C. Zhao, Y. Liu and Z. Ke, Enhanced Hydride Donation Achieved Molybdenum Catalyzed Direct N-Alkylation of Anilines or Nitroarenes with Alcohols: From Computational Design to Experiment, *ACS Catal.*, 2021, **11**, 10377–10382.
40 V. T. Nguyen, V. D. Nguyen, G. C. Haug, N. T. H. Vuong, H. T. Dang, H. D. Arman and O. V. Larionov, Visible-Light-Enabled Direct Decarboxylative N-Alkylation, *Angew. Chem., Int. Ed.*, 2020, **59**, 7921–7927.
41 S. Okumura, T. Komine, E. Shigeki, K. Semba and Y. Nakao, Site-Selective Linear Alkylation of Anilides by Cooperative Nickel/Aluminum Catalysis, *Angew. Chem., Int. Ed.*, 2018, **57**, 929–932.
42 C. Pinilla, V. Salamanca, A. Lledos and A. C. Albeniz, Palladium-Catalyzed Ortho C-H Arylation of Unprotected Anilines: Chemo- and Regioselectivity Enabled by the Cooperating Ligand [2,2′-Bipyridin]-6(1H)-one, *ACS Catal.*, 2022, **12**, 14527–14532.
43 S. Stiniya, P. V. Saranya and G. Anilkumar, An overview of iron-catalyzed N-alkylation reactions, *Appl. Organomet. Chem.*, 2021, **35**, e6444.
44 V. Sukowski, M. van Borselen, S. Mathew, B. de Bruin and M. A. Fernandez-Ibanez, meta-C-H Arylation of Aniline Derivatives via Palladium/S,O-Ligand/Norbornene Cooperative Catalysis, *Angew. Chem., Int. Ed.*, 2024, **63**, e202317741.
45 M. O. Tischler, M. B. Toth and Z. Novak, Mild Palladium Catalyzed ortho C-H Bond Functionalizations of Aniline Derivatives, *Chem. Rec.*, 2017, **17**, 184–199.

46 J. Wang, S. Li, C. Yang, H. Gao, L. Zuo, Z. Guo, P. Yang, Y. Jiang, J. Li, L. Z. Wu and Z. Tang, Photoelectrochemical Ni-catalyzed cross-coupling of aryl bromides with amine at ultra-low potential, *Nat. Commun.*, 2024, **15**, 6907.
47 S. Wang, G. Force, R. Guillot, J.-F. Carpentier, Y. Sarazin, C. Bour, V. Gandon and D. Lebœuf, Lewis Acid/Hexafluoroisopropanol: A Promoter System for Selective ortho-C-Alkylation of Anilines with Deactivated Styrene Derivatives and Unactivated Alkenes, *ACS Catal.*, 2020, **10**, 10794–10802.
48 Z. Xi, X.-J. Liu, Z. Guo, Z. Gao, Z.-X. Yu and H. Gao, Regioselective umpolung para-C–H functionalization of arylhydroxylamines, *Nat. Synth.*, 2023, **2**, 778–788.
49 J. Yang, Transition metal catalyzed meta-C-H functionalization of aromatic compounds, *Org. Biomol. Chem.*, 2015, **13**, 1930–1941.
50 C. Yuan, L. Zhu, C. Chen, X. Chen, Y. Yang, Y. Lan and Y. Zhao, Ruthenium(II)-enabled para-selective C-H difluoromethylation of anilides and their derivatives, *Nat. Commun.*, 2018, **9**, 1189.
51 J. F. Hartwig, Evolution of a fourth generation catalyst for the amination and thioetherification of aryl halides, *Acc. Chem. Res.*, 2008, **41**, 1534–1544.
52 L. Huang, M. Arndt, K. Goossen, H. Heydt and L. J. Goossen, Late transition metal-catalyzed hydroamination and hydroamidation, *Chem. Rev.*, 2015, **115**, 2596–2697.
53 H. Y. Bai, F. X. Tan, T. Q. Liu, G. D. Zhu, J. M. Tian, T. M. Ding, Z. M. Chen and S. Y. Zhang, Highly atroposelective synthesis of nonbiaryl naphthalene-1,2-diamine N-C atropisomers through direct enantioselective C-H amination, *Nat. Commun.*, 2019, **10**, 3063.
54 L. Wang, J. Zhou, T. M. Ding, Z. Q. Yan, S. H. Hou, G. D. Zhu and S. Y. Zhang, Asymmetric N-Hydroxyalkylation of Indoles with Ethyl Glyoxalates Catalyzed by a Chiral Phosphoric Acid: Highly Enantioselective Synthesis of Chiral N,O-Aminal Indole Derivatives, *Org. Lett.*, 2019, **21**, 2795–2799.
55 J. Zhou, G. D. Zhu, L. Wang, F. X. Tan, W. Jiang, Z. G. Ma, J. C. Kang, S. H. Hou and S. Y. Zhang, Remote C6-Enantioselective C-H Functionalization of 2,3-Disubstituted Indoles through the Dual H-Bonds and pi-pi Interaction Strategy Enabled by CPAs, *Org. Lett.*, 2019, **21**, 8662–8666.
56 C. Liu, F. X. Tan, J. Zhou, H. Y. Bai, T. M. Ding, G. D. Zhu and S. Y. Zhang, Highly Chemo-, Site-, and Enantioseletive para C-H Aminoalkylation of N-Monosubstituted Aniline Derivatives Affording 3-Amino-2-oxindoles, *Org. Lett.*, 2020, **22**, 2173–2177.
57 G. J. Wang, L. Wang, G. D. Zhu, J. Zhou, H. Y. Bai and S. Y. Zhang, Organocatalytic Direct Asymmetric Indolization from Anilines by Enantioselective [3 + 2] Annulation, *Org. Lett.*, 2021, **23**, 8434–8438.
58 G. J. Wang, S. Y. Zhang, Z. L. Sun, P. Li and T. M. Ding, Highly Site– and Enantioselective N—H Functionalization of N-Monosubstituted Aniline Derivatives Affording Pyrazolones Bearing a Quaternary Stereocenter, *Chin. J. Chem.*, 2022, **40**, 1144–1148.
59 Z.-H. Li, J. Zhou, C. Liu, F.-X. Tan, L. Wang, G.-D. Zhu and S.-Y. Zhang, How achiral Brønsted acid is involved in co-catalyst model with chiral phosphoric acid for construction of quaternary carbon stereocenter, *Chem Catal.*, 2024, **4**, 100918.
60 M. J. Frisch, G. W. Trucks, H. B. Schlegel, G. E. Scuseria, M. A. Robb, J. R. Cheeseman, G. Scalmani, V. Barone, G. A. Petersson, H. Nakatsuji, X. Li, M. Caricato, A. V. Marenich, J. Bloino, B. G. Janesko, R. Gomperts, B. Mennucci, H. P. Hratchian, J. V. Ortiz, A. F. Izmaylov, J. L. Sonnenberg, D. Williams-Young, F. Ding, F. Lipparini, F. Egidi, J. Goings, B. Peng, A. Petrone, T. Henderson, D. Ranasinghe, V. G. Zakrzewski, J. Gao, N. Rega, G. Zheng, W. Liang, M. Hada, M. Ehara, K. Toyota, R. Fukuda, J. Hasegawa, M. Ishida, T. Nakajima, Y. Honda, O. Kitao, H. Nakai, T. Vreven, K. Throssell, J. A. Montgomery Jr., J. E. Peralta, F. Ogliaro, M. J. Bearpark, J. J. Heyd, E. N. Brothers, K. N. Kudin, V. N. Staroverov, T. A. Keith, R. Kobayashi, J. Normand, K. Raghavachari, A. P. Rendell, J. C. Burant, S. S. Iyengar, J. Tomasi, M. Cossi, J. M. Millam, M. Klene, C. Adamo, R. Cammi, J. W. Ochterski, R. L. Martin, K. Morokuma, O. Farkas, J. B. Foresman and D. J. Fox, *Gaussian 16 Rev. A.03.Journal*, 2016.
61 Y. Zhao and D. G. Truhlar, The M06 suite of density functionals for main group thermochemistry, thermochemical kinetics, noncovalent interactions, excited states, and transition elements: two new functionals and systematic testing of four M06-class functionals and 12 other functionals, *Theor. Chem. Acc.*, 2007, **120**, 215–241.
62 M. M. Francl, W. J. Pietro, W. J. Hehre, J. S. Binkley, M. S. Gordon, D. J. DeFrees and J. A. Pople, Self-consistent molecular orbital methods. XXIII. A polarization-type basis set for second-row elements, *J. Chem. Phys.*, 1982, **77**, 3654–3665.
63 P. Pracht, F. Bohle and S. Grimme, Automated exploration of the low-energy chemical space with fast quantum chemical methods, *Phys. Chem. Chem. Phys.*, 2020, **22**, 7169–7192.
64 G. W. Spitznagel, T. Clark, P. von Ragué Schleyer and W. J. Hehre, An evaluation of the performance of diffuse function-augmented basis sets for second row elements, Na-Cl, *J. Comput. Chem.*, 1987, **8**, 1109–1116.
65 S. Grimme, J. Antony, S. Ehrlich and H. Krieg, A consistent and accurate ab initio parametrization of density functional dispersion correction (DFT-D) for the 94 elements H-Pu, *J. Chem. Phys.*, 2010, **132**, 154104.
66 A. V. Marenich, C. J. Cramer and D. G. Truhlar, Universal solvation model based on solute electron density and on a continuum model of the solvent defined by the bulk dielectric constant and atomic surface tensions, *J. Phys. Chem. B*, 2009, **113**, 6378–6396.
67 W. Humphrey, A. Dalke and K. Schulten, VMD: visual molecular dynamics, *J. Mol. Graphics*, 1996, **14**(33–38), 27–38.
68 T. Lu and F. Chen, Multiwfn: a multifunctional wavefunction analyzer, *J. Comput. Chem.*, 2012, **33**, 580–592.
69 C. Y. Legault, *CYLview20.Journal*, 2020.
70 T. Akiyama, Stronger Bronsted acids, *Chem. Rev.*, 2007, **107**, 5744–5758.

71 M. Terada, Chiral Phosphoric Acids as Versatile Catalysts for Enantioselective Transformations, *Synthesis*, 2010, 1929–1982.
72 Y. Wang, W. Chen, Y. Lai and A. Duan, Activation Model and Origins of Selectivity for Chiral Phosphoric Acid Catalyzed Diradical Reactions, *J. Am. Chem. Soc.*, 2023, **145**, 23527–23532.
73 R. Pino-Rios, D. Inostroza, G. Cardenas-Jiron and W. Tiznado, Orbital-Weighted Dual Descriptor for the Study of Local Reactivity of Systems with (Quasi-) Degenerate States, *J. Phys. Chem. A*, 2019, **123**, 10556–10562.
74 A. G. Green, P. Liu, C. A. Merlic and K. N. Houk, Distortion/Interaction analysis reveals the origins of selectivities in iridium-catalyzed C-H borylation of substituted arenes and 5-membered heterocycles, *J. Am. Chem. Soc.*, 2014, **136**, 4575–4583.
75 F. M. Bickelhaupt and K. N. Houk, Analyzing Reaction Rates with the Distortion/Interaction-Activation Strain Model, *Angew. Chem., Int. Ed.*, 2017, **56**, 10070–10086.
76 F. Liu, Y. Liang and K. N. Houk, Bioorthogonal Cycloadditions: Computational Analysis with the Distortion/Interaction Model and Predictions of Reactivities, *Acc. Chem. Res.*, 2017, **50**, 2297–2308.
77 I. O. Betinol, J. Lai, S. Thakur and J. P. Reid, A Data-Driven Workflow for Assigning and Predicting Generality in Asymmetric Catalysis, *J. Am. Chem. Soc.*, 2023, **145**, 12870–12883.
78 A. Duan, J. S. Fell, P. Yu, C. Y. Lam, M. Gravel and K. N. Houk, Theoretical Study of Diastereoselective NHC-Catalyzed Cross-Benzoin Reactions between Furfural and N-Boc-Protected alpha-Amino Aldehydes, *J. Org. Chem.*, 2019, **84**, 13565–13571.
79 A. Duan, P. Yu, F. Liu, H. Qiu, F. L. Gu, M. P. Doyle and K. N. Houk, Diazo Esters as Dienophiles in Intramolecular (4 + 2) Cycloadditions: Computational Explorations of Mechanism, *J. Am. Chem. Soc.*, 2017, **139**, 2766–2770.
80 A. Duan, Y. Yu, F. Wang, X. Wang and D. Wang, Mechanism and Origin of Stereoselectivity of Ni-Catalyzed Cyclization/Carboxylation of Bromoalkynes with CO(2), *J. Org. Chem.*, 2022, **87**, 8342–8350.
81 J. Klein, H. Khartabil, J. C. Boisson, J. Contreras-Garcia, J. P. Piquemal and E. Henon, New Way for Probing Bond Strength, *J. Phys. Chem. A*, 2020, **124**, 1850–1860.
82 A. Duan, F. Xiao, Y. Lan and L. Niu, Mechanistic views and computational studies on transition-metal-catalyzed reductive coupling reactions, *Chem. Soc. Rev.*, 2022, **51**, 9986–10015.
83 R. A. Oshiya and A. Datta, Machine learning for predicting enantioselectivity in chiral phosphoric acid-catalyzed naphthyl-indole synthesis, *J. Chem. Sci.*, 2025, **137**, 28.
84 S. E. Wheeler and K. N. Houk, Substituent effects in the benzene dimer are due to direct interactions of the substituents with the unsubstituted benzene, *J. Am. Chem. Soc.*, 2008, **130**, 10854–10855.
85 J. A. Read, T. E. Ball, B. R. Miller, E. N. Jacobsen and M. S. Sigman, Computational Library Enables Pattern Recognition of Noncovalent Interactions and Application as a Modern Linear Free Energy Relationship, *J. Org. Chem.*, 2024, **89**, 17237–17247.

